Current Applied Physics 14 (2014) 1263–1272

Contents lists available at ScienceDirect

Current Applied Physics

journal homepage: www.elsevier.com/locate/cap

Numerical analysis of energy-minimizing wavelengths of equilibrium states for diblock copolymers

Darae Jeong [a], Jaemin Shin [b], Yibao Li [c], Yongho Choi [a], Jae-Hun Jung [d], Seunggyu Lee [a], Junseok Kim [a,*]

[a] Department of Mathematics, Korea University, Seoul 136-713, Republic of Korea
[b] Institute of Mathematical Sciences, Ewha W. University, Seoul 120-750, Republic of Korea
[c] Department of Computational Science and Engineering, Yonsei University, Seoul, 120-749, Republic of Korea
[d] Department of Mathematics, State University of New York at Buffalo, Buffalo, NY 14260-2900, United States

ARTICLE INFO

Article history:
Received 23 April 2014
Received in revised form
13 June 2014
Accepted 17 June 2014
Available online 8 July 2014

Keywords:
Nonlocal Cahn–Hilliard equation
Lamellar phase
Wavelength
Phase separation
Diblock copolymer

ABSTRACT

We present a robust and accurate numerical algorithm for calculating energy-minimizing wavelengths of equilibrium states for diblock copolymers. The phase-field model for diblock copolymers is based on the nonlocal Cahn–Hilliard equation. The model consists of local and nonlocal terms associated with short- and long-range interactions, respectively. To solve the phase-field model efficiently and accurately, we use a linearly stabilized splitting-type scheme with a semi-implicit Fourier spectral method. To find energy-minimizing wavelengths of equilibrium states, we take two approaches. One is to obtain an equilibrium state from a long time simulation of the time-dependent partial differential equation with varying periodicity and choosing the energy-minimizing wavelength. The other is to directly solve the ordinary differential equation for the steady state. The results from these two methods are identical, which confirms the accuracy of the proposed algorithm. We also propose a simple and powerful formula: $h = L^*/m$, where h is the space grid size, L^* is the energy-minimizing wavelength, and m is the number of the numerical grid steps in one period of a wave. Two- and three-dimensional numerical results are presented validating the usefulness of the formula without trial and error or ad hoc processes.

1. Introduction

A diblock copolymer is a polymer consisting of a block of one type of monomer, A, joined chemically to a block of another type of monomer, B [1]. Below a critical temperature, the two sequences are incompatible and the copolymer melt undergoes phase separation [2]. This occurs on the mesoscopic scale and the observed mesoscopic domains show periodic structures including lamellae, spheres, cylinders, and gyroids [3]. These phase separations have been observed experimentally [4–16], studied mathematically [3,17–26], and simulated numerically [27–39]. For the mathematical approach to phase separation, dynamic mean field theory, based on the self-consistent field theory [40,41], has been widely studied. In this work, we use the density functional theory proposed by Ohta and Kawasaki [24]. This is dependent on the monomer density [42], which is the minimization of a nonlocal Cahn–Hilliard (CH) free energy defined by an order parameter. Here, a diblock copolymer is described by the order parameter ϕ, which represents the relative local density difference between two monomers constituting the copolymer. The standard CH free energy, generally used for the modeling of phase separation [43], is supplemented with a nonlocal term [44].

Numerical experiments are useful to predict self-assembly structures of the diblock copolymer, containing lamellae, spheres, and cylindrical tubes. However, because of the non-convexity of the Ohta–Kawasaki functional, the numerical results can draw the metastable state and local minimizer. We would like to refer [45] for the study on assessing the lowest energy state and escaping from certain metastable states by using a spectral weighting. Although there have been a number of numerical studies on diblock copolymer phase separation, there has been little investigation of the accurate calculation of the energy-minimizing wavelengths of equilibrium states. Therefore, the main purpose of this paper is to develop a robust and accurate numerical algorithm for calculating the energy-minimizing wavelengths of equilibrium states in diblock copolymers. We also propose a simple and powerful

* Corresponding author. Tel.: +82 2 3290 3077; fax: +82 2 929 8562.
E-mail address: cfdkim@korea.ac.kr (J. Kim).
URL: http://math.korea.ac.kr/%4ecfdkim

http://dx.doi.org/10.1016/j.cap.2014.06.016
1567-1739/

formula for the space grid size. This controllability of the space step size is essential in the computational simulations for the physical experiments.

This paper is organized as follows. In Section 2, we briefly describe a phase field model of diblock copolymer. In Section 3, we present a linearly stabilized splitting-type scheme with a semi-implicit Fourier spectral method to solve the phase-field model efficiently and accurately. In Section 4, we perform a series of numerical experiments. Finally, our conclusion and discussion are given in Section 5.

2. Mathematical model

We consider a diblock copolymer consisting of two homopolymer blocks A and B. The governing equation is the Ohta–Kawasaki model [24]. Let the order parameter $\phi(\mathbf{x}) = \rho_A(\mathbf{x}) - \rho_B(\mathbf{x})$ be defined as the difference between the local volume fractions of A and B at the point $\mathbf{x}$. The governing equation is the following partial differential equation (PDE),

$$\frac{\partial \phi(\mathbf{x},t)}{\partial t} = \Delta\Big(F'(\phi(\mathbf{x},t)) - \varepsilon^2\Delta\phi(\mathbf{x},t)\Big) - \alpha\big(\phi(\mathbf{x},t) - \overline{\phi}\big), \tag{1}$$

where $\mathbf{x}\in\Omega\subset\mathbf{R}^d$ $(d = 1,2,3)$ is the domain, $F(\phi) = 0.25(\phi^2-1)^2$ is the Helmholtz free energy, ε is the gradient energy coefficient, α is inversely proportional to the square of the total chain length of the copolymer [46], and $\overline{\phi} = \int_\Omega \phi(\mathbf{x},0)d\mathbf{x}/\int_\Omega d\mathbf{x}$ is the total mass. We now briefly review the derivation of Eq. (1). The free energy functional is represented as the sum of two parts as $\varepsilon_{\text{total}} = \varepsilon_{\text{short}} + \varepsilon_{\text{long}}$. First, $\varepsilon_{\text{short}}(\phi)$ denotes the short-range part of the free energy functional,

$$\varepsilon_{\text{short}}(\phi) := \int_\Omega \left(F(\phi) + \frac{\varepsilon^2}{2}|\nabla\phi|^2\right)d\mathbf{x}.$$

Second, $\varepsilon_{\text{long}}(\phi)$ denotes the long-range part of the free energy functional,

$$\varepsilon_{\text{long}}(\phi) := \frac{\alpha}{2}\int_\Omega\int_\Omega G(\mathbf{x}-\mathbf{y})\big(\phi(\mathbf{x}) - \overline{\phi}\big)\big(\phi(\mathbf{y}) - \overline{\phi}\big)d\mathbf{y}d\mathbf{x},$$

where G is the Green's function having the following property: $\Delta G(\mathbf{x}-\mathbf{y}) = -\delta(\mathbf{x}-\mathbf{y})$. Here, periodic boundary conditions are assumed and δ is Dirac delta function. By taking a variational derivative and letting $f = F'$, we have,

$$\frac{\delta\varepsilon_{\text{short}}(\phi)}{\delta\phi} = f(\phi) - \varepsilon^2\Delta\phi, \tag{2}$$

$$\frac{\delta\varepsilon_{\text{long}}(\phi)}{\delta\phi} = \alpha\int_\Omega G(\mathbf{x}-\mathbf{y})\big(\phi(\mathbf{y}) - \overline{\phi}\big)d\mathbf{y}. \tag{3}$$

Next, we deduce Eq. (1) by substituting Eqs. (2) and (3) into the evolution equation.

$$\phi_t = \Delta\left(\frac{\delta\varepsilon_{\text{short}}(\phi)}{\delta\phi} + \frac{\delta\varepsilon_{\text{long}}(\phi)}{\delta\phi}\right) = \Delta\Big(f(\phi) - \varepsilon^2\Delta\phi\Big) - \alpha\big(\phi - \overline{\phi}\big).$$

Note that if ψ satisfies $-\Delta\psi = \phi - \overline{\phi}$ with the periodic boundary condition [3], then we can represent $\varepsilon_{\text{long}}(\phi)$ as,

$$\varepsilon_{\text{long}}(\phi) = \frac{\alpha}{2}\int_\Omega \Delta_{\mathbf{x}}\psi(\mathbf{x})\left[\int_\Omega \Delta_{\mathbf{y}}G(\mathbf{x}-\mathbf{y})\psi(\mathbf{y})d\mathbf{y}\right]$$
$$d\mathbf{x} = \frac{\alpha}{2}\int_\Omega |\nabla\psi(\mathbf{x})|^2 d\mathbf{x}.$$

Therefore, an alternative form of the total system energy is given as,

$$\varepsilon_{\text{total}}(\phi) = \int_\Omega \left(F(\phi) + \frac{\varepsilon^2}{2}|\nabla\phi|^2\right)d\mathbf{x} + \frac{\alpha}{2}\int_\Omega |\nabla\psi|^2 d\mathbf{x},$$

which we will use for the numerical evaluation of the total energy. Differentiate the energy $\varepsilon_{\text{total}}$ and the total mass $\int_\Omega \phi d\mathbf{x}$ with respect to time, and using the periodic boundary condition, we have,

$$\frac{d}{dt}\varepsilon_{\text{total}}(t) = -\int_\Omega |\nabla(\mu + \alpha\psi)|^2 d\mathbf{x} \le 0 \quad \text{and} \quad \frac{d}{dt}\int_\Omega \phi d\mathbf{x} = 0,$$

where $\mu = f(\phi) - \varepsilon^2\Delta\phi$. Therefore, the total energy is non-increasing and the total mass is conserved in time.

3. Numerical solution

In this section, we present a fully discrete scheme for the following one-dimensional nonlocal CH equation with the periodic boundary condition on $\Omega = (0,L)$:

$$\frac{\partial\phi(x,t)}{\partial t} = \frac{\partial^2 f(\phi(x,t))}{\partial x^2} - \varepsilon^2\frac{\partial^4\phi(x,t)}{\partial x^4} - \alpha\big(\phi(x,t) - \overline{\phi}\big). \tag{4}$$

We use the equidistant grid $x_m = (m-1)h$ for $m = 1,\ldots,M$ where M is an even number and $h = L/M$. Let ϕ_m^n be an approximation of $\phi(x_m, n\Delta t)$, where Δt is the temporal step size. We define the grid function $\phi^n = (\phi_1^n,\ldots,\phi_M^n)$ as a vector of grid point values. In particular, we denote the constant vector as $1 = (1,\ldots,1)$. The discrete Fourier transform and its inverse transform are defined by,

$$\widehat{\phi}_p^n = \sum_{m=1}^{M}\phi_m^n e^{-ix_m\xi_p}, \tag{5}$$

$$\phi_m^n = \frac{1}{M}\sum_{p=1-M/2}^{M/2}\widehat{\phi}_p^n e^{ix_m\xi_p}, \tag{6}$$

where $\xi_p = 2\pi(p-1)/L$. The second- and fourth-order partial derivatives are,

$$\frac{\partial^2\phi}{\partial x^2} = -\frac{1}{M}\sum_{p=1-M/2}^{M/2}\xi_p^2\widehat{\phi}_p^n e^{ix\xi_p}, \frac{\partial^4\phi}{\partial x^4} = \frac{1}{M}\sum_{p=1-M/2}^{M/2}\xi_p^4\widehat{\phi}_p^n e^{ix\xi_p}.$$

To solve Eq. (4), we use the linearly stabilized splitting-type scheme [47] with a semi-implicit Fourier spectral method [33,48–50]. The linear terms are treated implicitly and the nonlinear term is treated explicitly,

$$\frac{\phi_m^{n+1} - \phi_m^n}{\Delta t} = 2\frac{\partial^2\phi_m^{n+1}}{\partial x^2} - \varepsilon^2\frac{\partial^4\phi_m^{n+1}}{\partial x^4} + \frac{\partial^2 g_m^n}{\partial x^2} - \alpha\Big(\phi_m^{n+1} - \overline{\phi}\Big), \tag{7}$$

where $g_m^n = f(\phi_m^n) - 2\phi_m^n$ and $\overline{\phi} = \sum_{m=1}^M \phi_m^0/M$. If $\alpha = 0$, then Eq. (7) becomes the linear stabilized scheme for the CH equation [47]. For the higher temporal order spectral scheme of the nonlocal CH

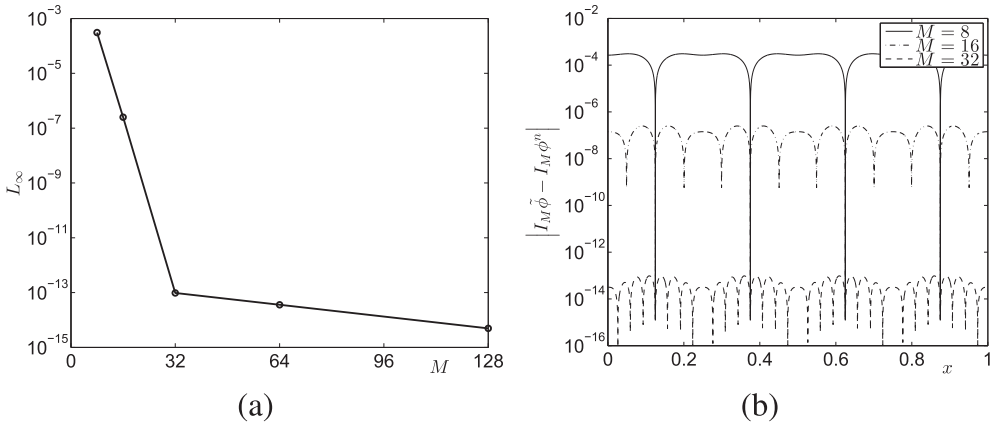

Fig. 1. (a) Maximum error of the numerical solution, measured at $t = 10^{-2}$. (b) Pointwise approximation error for increasing resolution.

equation, please refer to [51]. Using Eq. (6), Eq. (7) can be transformed into the discrete Fourier space as follows:

$$\widehat{\phi}_p^{n+1} = \frac{\widehat{\phi}_p^n - \Delta t\xi_p^2\widehat{g}_p^n + \alpha\Delta t\overline{\phi}\widehat{1}_p}{1 + \alpha\Delta t + 2\Delta t\xi_p^2 + \varepsilon^2\Delta t\xi_p^4}. \tag{8}$$

After updating $\widehat{\phi}_p^{n+1}$ with $\widehat{\phi}_p^n$, we recover ϕ_m^{n+1} from $\widehat{\phi}_p^{n+1}$ by the inverse discrete Fourier transform, Eq. (6). To satisfy the mass conservation property, we should have $\sum_{m=1}^M \phi_m^{n+1} = \sum_{m=1}^M \phi_m^n$. By using Eq. (5), we only need to prove $\widehat{\phi}_1^{n+1} = \widehat{\phi}_1^n$. From Eq. (8), we get $\widehat{\phi}_1^1 = (\widehat{\phi}_1^0 + \alpha\Delta tM\overline{\phi})/(1+\alpha\Delta t) = (\widehat{\phi}_1^0 + \alpha\Delta t\widehat{\phi}_1^0)/(1+\alpha\Delta t) = \widehat{\phi}_1^0$. Here, we have used the definitions of $\overline{\phi}$ and Fourier transform. If $\widehat{\phi}_1^n = \widehat{\phi}_1^0$, we have $\widehat{\phi}_1^{n+1} = (\widehat{\phi}_1^n + \alpha\Delta tM\overline{\phi})/(1+\alpha\Delta t) = (\widehat{\phi}_1^0 + \alpha\Delta t\widehat{\phi}_1^0)/(1+\alpha\Delta t) = \widehat{\phi}_1^0$. Therefore, we can get $\widehat{\phi}_1^n = \widehat{\phi}_1^0$ for all n. Thus, our proposed scheme inherits the mass conservation. Let the Fourier interpolation of ϕ^n be $I_M\phi^n(x) = \frac{1}{M}\sum_{p=1-M/2}^{M/2}\widehat{\phi}_p^n e^{ix\xi_p}$. We define the discrete energy as $\varepsilon_{\text{total}}^h(\phi^n) = \varepsilon_{\text{short}}^h(\phi^n) + \varepsilon_{\text{long}}^h(\phi^n)$, where,

$$\varepsilon_{\text{short}}^h(\phi^n) = h\sum_{m=1}^M\left[F(\phi_m^n) + \frac{\varepsilon^2}{2}\left(\frac{d}{dx}I_M\phi^n(x_m)\right)^2\right],$$

$$\varepsilon_{\text{long}}^h(\phi^n) = h\sum_{m=1}^M\frac{\alpha}{2}\left(\frac{d}{dx}I_M\psi^n(x_m)\right)^2.$$

Here, we use the Fourier spectral method to solve the Poisson equation $-\frac{\partial^2\psi_m^n}{\partial x^2} = \phi_m^n - \overline{\phi}$. Note that we set $\widehat{\psi}_1^n = 0$ to guarantee a unique solution. We also perform the numerical simulation for the nonlocal CH equation on two- and three-dimensional domains $\Omega = (0,L)^d$, $d = 2,3$, using a multigrid method for the CH equation [52,53].

4. Numerical experiments

In this section, we describe a series of numerical experiments. We perform a convergence test and a linear stability analysis, calculate the discrete total energy dissipation and distribution at equilibrium states, compute the optimal wavelength with the minimum discrete total energy, study the effect of α, ε, and $\overline{\phi}$, and compare the PDE solver with an ordinary differential equation (ODE) solver. We implement two- and three-dimensional numerical experiments using the new formula for an optimal grid spacing. Throughout the experiments, unless otherwise specified, we use $\varepsilon = 1/(20\sqrt{2})$, $\alpha = 100$, $h = 0.00125$, and $\Delta t = 0.0625$.

4.1. Numerical convergence test

We examine the convergence of our proposed scheme. The initial state is $\phi(x,0) = 0.1\cos(4\pi x)$ in $\Omega = (0,1)$. To calculate the accuracy of the proposed method, the numerical solutions ϕ^n are computed on the grids $M = 2^s$ for $s = 3,4,\ldots,7$. For each case, the calculation is run until $T = 10^{-2}$ with the time step $\Delta t = 10^{-6}$ and $\varepsilon = 0.05$. We define the error of a grid to be the maximum pointwise error, given by $L_\infty = \max|I_M\bar{\phi} - I_M\phi^n|$. We define $\bar{\phi}$ as the reference solution, which is the numerical solution using $M = 2^{10}$ grid points. Fig. 1(a and b) show the maximum errors and pointwise error of approximation for increasing resolution, respectively. As can be seen, the convergence of the results under mesh refinements is evident.

4.2. Discrete total energy dissipation

Fig. 2 illustrates the temporal evolutions of the normalized discrete total energy $\varepsilon_{\text{total}}^h(t)/\varepsilon_{\text{total}}^h(0)$ and the total mass until $T = 20$ with $M = 800$. The initial condition is $\phi(x,0) = 0.1\text{r}$ and(x) with the zero average $\overline{\phi} = 0$ in $\Omega = (0,1)$, where rand(x) is a random value between -1 and 1. Fig. 2(a) shows that the discrete total energy

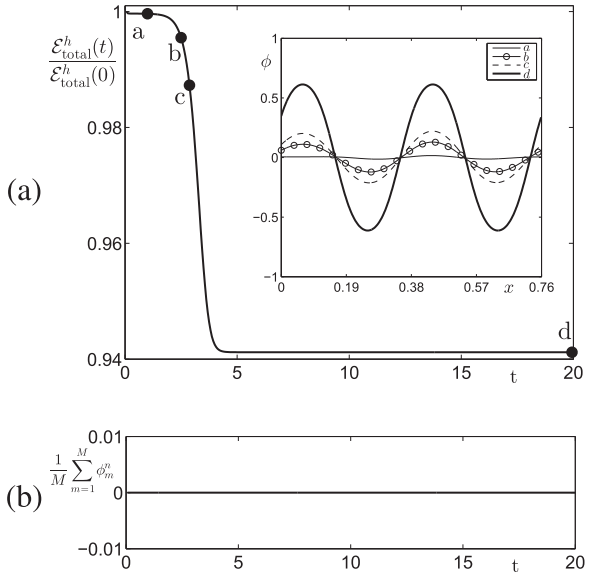

Fig. 2. Temporal evolutions of (a) the normalized discrete total energy $\varepsilon_{\text{total}}^h(t)/\varepsilon_{\text{total}}^h(0)$ and (b) the total mass $\sum_{m=1}^M \phi_m^n/M$.

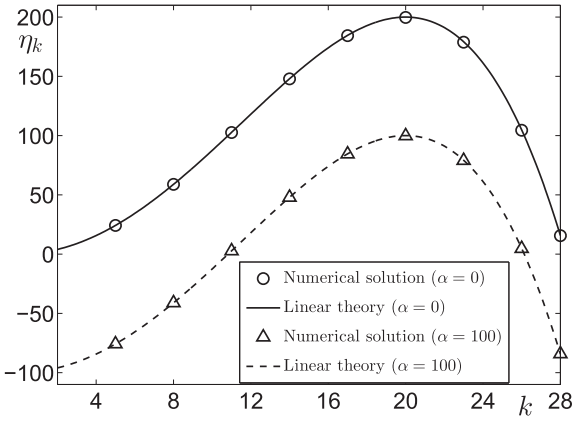

Fig. 3. Growth rate given by linear stability theory and numerical solution as a function of k with $\alpha = 0$ and $\alpha = 100$.

decreases and dots are associated with profiles in the inserted chart. Fig. 2(b) confirms that the total mass is preserved.

4.3. Linear stability analysis

We examine the linear stability of the trivial stationary solution $\phi = \overline{\phi}$ on the one-dimensional space. Under a linear stability analysis [2,44,54], the solution of Eq. (1) is assumed to have the form,

$$\phi(x,t) = \overline{\phi} + \sum_{k=1}^{\infty} \beta_k(t)\cos(kx), \tag{9}$$

where $|\beta_k(t)| \ll 1$. Substituting Eq. (9) into Eq. (1), we have,

$$\frac{d\beta_k}{dt} = -k^2\left[3\overline{\phi}^2 - 1 + \varepsilon^2 k^2\right]\beta_k + \alpha\beta_k, \tag{10}$$

up to first order. The solution of Eq. (10) is $\beta_k(t) = \beta_k(0)\exp(\eta_k t)$, where $\eta_k = -k^2[3\overline{\phi}^2 - 1 + \varepsilon^2 k^2] - \alpha$ is the growth rate. Therefore, we have the maximal growth rate if we take the wavenumber as $k_{\max} = \sqrt{1 - 3\overline{\phi}^2}/(\sqrt{2}\varepsilon)$. Note that this is independent of the value of α. Next, the theoretical growth rate η_k is compared to the numerical growth rate given by our proposed scheme for different values of k and α. The numerical growth rate is defined by $\tilde{\eta}_k = \log(\max_{1\le m\le M}|\phi_m^n| / \max_{1\le m\le M}|\phi_m^0|)/T$. For the numerical test, we take the initial condition $\phi(x,0) = 0.01\cos(kx)$ on $\Omega = (0,2\pi)$. With

Table 1
Optimal length L^* with varying h and fixed $\Delta t = 0.1$.

h	L^*
0.010000	0.375111392605260
0.005000	0.374721801635760
0.002500	0.374711672256741
0.001250	0.374687609705082
0.000625	0.374681591974566

Table 2
Optimal length L^* with varying Δt and fixed $h = 0.00125$.

Δt	L^*
1.0000	0.374687609705025
0.5000	0.374687609705055
0.2500	0.374687609705065
0.1250	0.374687609705054
0.0625	0.374687609705047

$\Delta t = 10^{-6}$, the numerical simulations are run up to $T = n\Delta t = 10^{-4}$. Fig. 3 suggests that the theoretical values from the linear analysis (solid ($\alpha = 0$) and dashed ($\alpha = 100$) lines) and the numerical results (circle ($\alpha = 0$) and triangle ($\alpha = 100$) symbols) are in good agreement. Moreover, the numerical result shows that the growth rate is maximum at $k = 20$, which is consistent with the theoretical result.

4.4. Discrete total energy at equilibrium states

We define the numerical solution to be in the steady state, when the consecutive error is less than a given tolerance, tol, $\max_{1\le m\le M}|\phi_m^{n+1} - \phi_m^n|/\Delta t < \text{tol}$. From now on, we will use tol $= 10^{-12}$. We calculate the domain-size-scaled discrete total energy $\varepsilon_{\text{total}}^h/L$ with an equilibrium solution in $(0,L)$. The numerical result in Fig. 4 shows $\varepsilon_{\text{total}}^h/L$ as a function of L. The initial condition is taken as $\phi(x,0) = 0.1$ rand (x) and shown in the jagged lines. The inscribed figures correspond to equilibrium state profiles at the indicated domain sizes. We can observe that the domain-size-scaled discrete total energy is minimized when $L \approx 0.38$ (one wave) and 0.76 (two waves). This doubling length is due to the periodic boundary condition.

4.5. Optimal length L^* having minimum discrete total energy $\varepsilon_{total}^h/L^*$

We describe an algorithm for finding the total energy-minimizing wavelength. We define the optimal length L^* as the

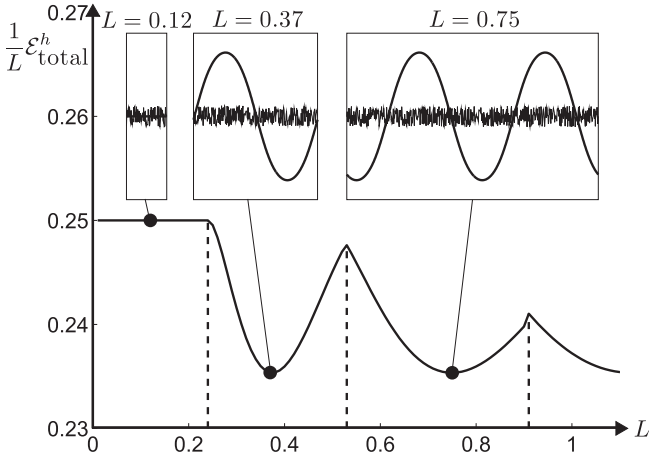

Fig. 4. Domain-size-scaled discrete total energy $\varepsilon_{\text{total}}^h/L$ as a function of L.

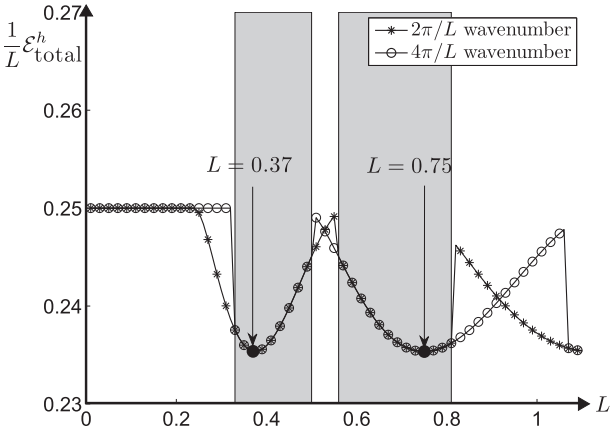

Fig. 5. Local minimum of $\varepsilon_{\text{total}}^h/L$ regardless of the initial wavenumbers.

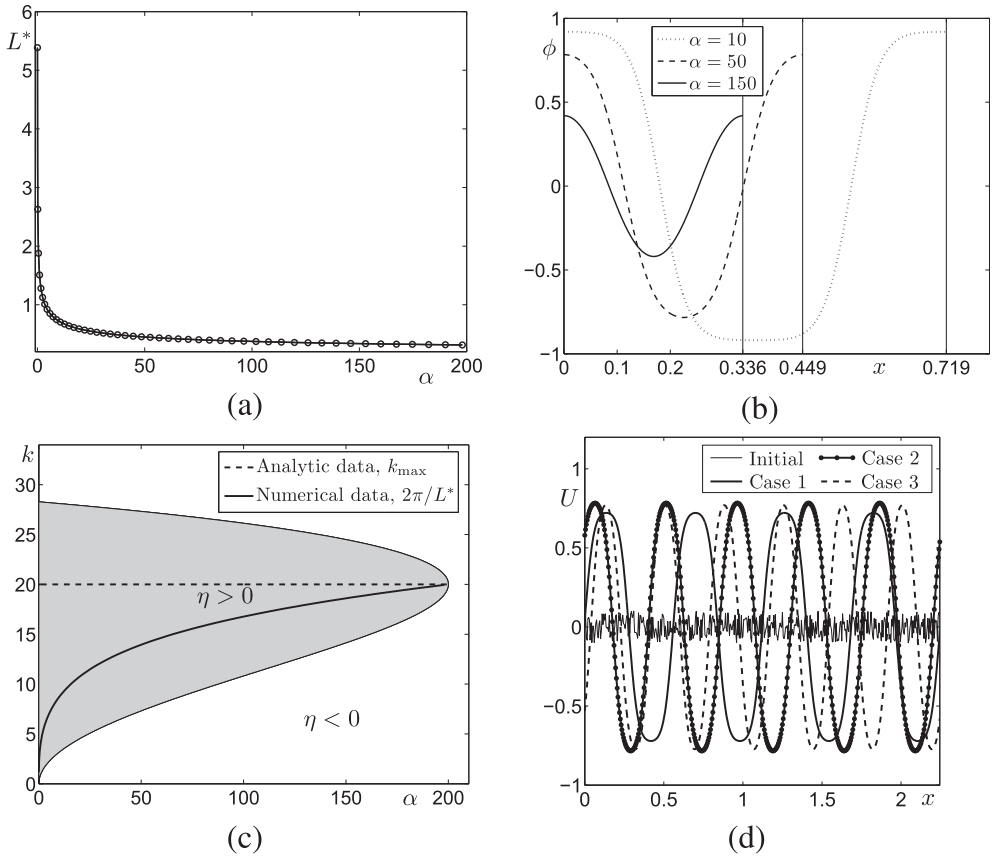

Fig. 6. (a) Optimal length L^* as a function of the value of α. (b) Equilibrium states with varying α. (c) Comparison between linear stability theory and numerical simulation results. (d) Various equilibrium states with $\alpha = 50$ and $L = 5L^*$.

smallest length having the global minimum of scaled discrete total energy. To calculate L^*, we solve Eq. (7) until it reaches a numerical equilibrium state with given values of h, Δt, ε, and α. The initial condition is $\phi(x,0) = 0.01\cos(2\pi x/L)$ in $\Omega = (0,L)$, where L starts at 2 h and increases in steps of 2 h. Let M be the smallest even integer such that $\varepsilon^h_{\text{total}}/(Mh)$ is minimized in $\Omega = (0,Mh)$. Construct the quadratic polynomial passing the three points $((M-2)h, \varepsilon^h_{\text{total}}/((M-2)h))$, $(Mh, \varepsilon^h_{\text{total}}/(Mh))$, and $((M+2)h, \varepsilon^h_{\text{total}}/((M+2)h))$, then define the optimal length L^* as the critical point of the polynomial.

Table 1 shows the optimal length L^* for varying h with $\Delta t = 0.1$. The result indicates that the solution with $h = 0.00125$ is sufficiently accurate. We also tested the effect of the time step Δt on the optimal length L^* (see Table 2). We will use $h = 0.00125$ and $\Delta t = 0.0625$ in the subsequent sections.

4.6. Initial wavenumber-independent local minimum of ε^h_{total}/L

We show that the domain-size-scaled discrete total energy $\varepsilon^h_{\text{total}}/L$ has the same energy-minimizing wavelength which is independent on the initial wavenumbers. For this numerical simulation, we use the two different initial conditions as $\phi(x,0) = 0.5\cos(2\pi x/L)$ and $\phi(x,0) = 0.5\cos(4\pi x/L)$ in $(0,L)$. Fig. 5 shows $\varepsilon^h_{\text{total}}/L$ as a function of L with two different initial

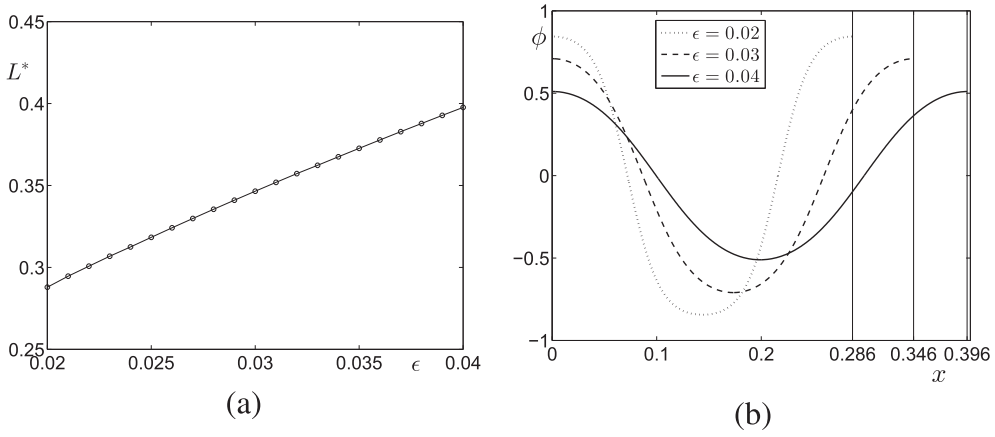

Fig. 7. (a) Optimal length L^* against ε. (b) Profiles of ϕ at the equilibrium state when $\varepsilon = 0.02$,0.03, and 0.04.

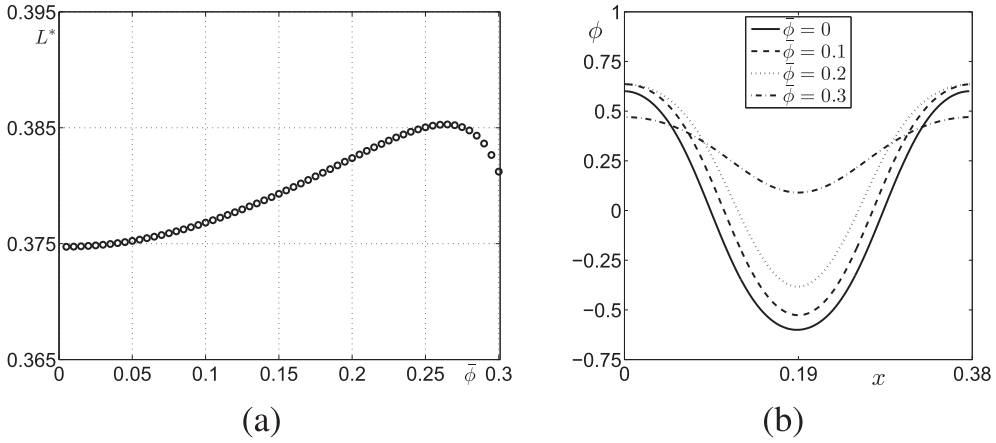

Fig. 8. (a) Effect of $\bar{\phi}$ on the optimal length L^*. (b) Steady state phase-field profiles for different $\bar{\phi}$.

wavenumbers which are indicated by the star line ($2\pi/L$ wavenumber) and circled line ($4\pi/L$ wavenumber). In Fig. 5, the domain-size-scaled discrete total energy is minimized at the same wavelengths $L \approx 0.37$ and 0.75 regardless of the initial wavenumbers. The shaded areas containing $L = 0.37$ and $L = 0.75$ represent one and two period of waves, respectively.

4.7. Effect of α on L^*

Fig. 6(a) shows the optimal length L^* as a function of the value of the long-range interaction parameter α. Here, we use the initial condition $\phi(x,0) = 0.01\cos(2\pi x/L)$. The energy-minimizing wavelength becomes shorter as α increases. Fig. 6(b) shows equilibrium profiles with $\alpha = 10$,50, and 150. It also shows that the wave amplitude decreases as α increase. In Fig. 6(c), the shaded region is the positive growth phase plane of α and wavenumber k. The dashed line is the maximum growth wavenumber of the linear stability analysis, and the thick solid line is the numerical simulation result, $2\pi/L^*$, with varying α. As α approaches 200, $2\pi/L^*$ converges to 20. Fig. 6(d) represents three cases of different equilibrium states with different random initial conditions. Here, $\alpha = 50$, $L = 5L^*$, and $h = 0.00125$ are used. When $L = 5L^*$, we expect the energy minimizing steady solution is a five-periodic wave. However, as shown in Fig. 6(d), the steady state solutions are four-, five-, or six-periodic waves. These phenomena can be explained from Fig. 6(c). There are many growing modes other than the energy minimizing mode. This implies that we could have different equilibrium solutions form different initial conditions.

4.8. Effect of ε on L^*

Fig. 7(a) shows the optimal length L^* as a function of the value of ε. Here, we use the initial condition $\phi(x,0) = 0.01\cos(2\pi x/L)$. We can observe that the energy minimizing wavelength L^* also increases as ε increases. Fig. 7(b) shows profiles of ϕ at equilibrium state when $\varepsilon = 0.02$, 0.03, and 0.04. We also observe that the amplitude of the phase-field is smaller as ε increases.

4.9. Effect of $\bar{\phi}$ on L^*

Fig. 8(a) illustrates the effect of $\bar{\phi}$ on the optimal length L^*. Here, we use the initial condition $\phi(x,0) = 0.01\cos(2\pi x/L) + \bar{\phi}$. As shown in Fig. 8(a), the values of L^* increase from $\bar{\phi} = 0$ to $\bar{\phi} = 0.26$, and then decrease when the total mass $\bar{\phi}$ is larger than 0.26. Fig. 8(b) shows the steady state phase-field profiles for different $\bar{\phi}$.

4.10. Comparison of results from PDE and ODE

We compare the steady state solutions given by two methods to show that the results are reliable. The first method solves the steady state equation of Eq. (1) using a MATLAB (ver. 7.14, R2012b, The Mathworks, Inc., MA) solver bvp5c [55–57]. The equilibrium solution for Eq. (1) should satisfy,

$$\left(\phi^3 - \phi - \varepsilon^2\phi_{xx}\right)_{xx} - \alpha\phi = 0, \quad x \in (0, L),$$

which is subject to the periodic boundary conditions,

$$\phi(0) = \phi(L) = 0,\ \phi_x(0) = \phi_x(L),\ \phi_{xx}(0) = \phi_{xx}(L),\ \phi_{xxx}(0) = \phi_{xxx}(L).$$

The second method is to evolve Eq. (1) until it reaches the steady state. Fig. 9 shows the steady state solutions for different initial conditions. The initial states are $0.5\sin(2\pi x/L)$ and $0.9\sin(2\pi x/L)$, where $L = 0.38$. For the evolution, we use $M = 64$. The solid line is the solution obtained by the ODE solver, and the circles are those given by the Fourier spectral method. From this result, we can confirm that the steady solution from the PDE does not become stuck in a metastable state that has a larger total energy than the global minimizers.

We have an equilibrium solution $\phi(x) = \tanh[x/(\sqrt{2}\varepsilon)]$ on the infinite domain when $\alpha = 0$. Therefore, ϕ varies from -0.9 to 0.9 over a distance of about $2\sqrt{2}\varepsilon\tanh^{-1}(0.9)$. If $\varepsilon = hm/2\sqrt{2}\tanh^{-1}(0.9)$, then we have approximately m grid points across the

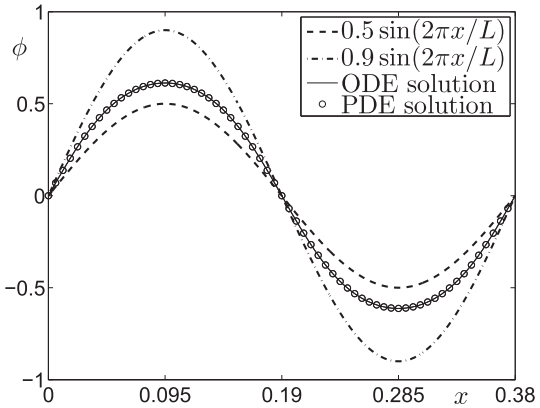

Fig. 9. Steady state solutions from PDE and ODE with two different initial configurations.

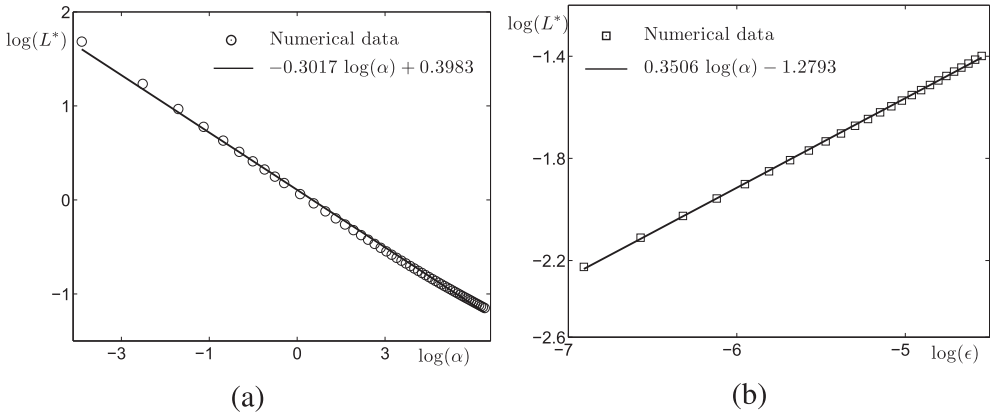

Fig. 10. (a) and (b) are linear fittings of $\log(L^*)$ versus the values of $\log(\alpha)$ and $\log(\varepsilon)$, respectively.

interfacial transition layer [58]. However, there is no non-trivial closed-form solution of the nonlocal CH equation ($\alpha \neq 0$). We propose the following simple and powerful formula: if we want to have m numerical grid steps in one period of a wave, we define $h = L^*/m$, where L^* is the energy minimizing optimal length. This controllability of the numerical grid steps is very important in the computational simulations for the physical experiments. For example, if h is too large, it is difficult to get sufficiently resolved numerical results. On the other hand, if h is too small, large scale computations are extremely costly for higher-dimensional (2D or 3D) simulations. Therefore, the proposed formula for the choice of the spatial step size h will be useful to do accurate and efficient numerical simulations without trial and error or ad hoc processes.

4.11. Scaling law for L^* in terms of α and ε

In this section, we numerically investigate the scaling law for L^* in terms of α and ε. In Ref. [44], the authors presented a formula for L^* with $\overline{\phi} = 0$ as,

$$L^* = \left(\frac{64\sqrt{2}\varepsilon}{\alpha}\right)^{1/3} + O\left(\varepsilon^{2/3}\right).$$

First, we fix the value of ε as $1/(20\sqrt{2})$ and change α from 0 to 200. As shown in Fig. 10(a), we find the following linear fitting: $log(L^*) = -0.3017\log(\alpha) + 0.3983$, which is close to the theoretical prediction. Next, we fix $\alpha = 100$ and change the value of ε from 0.001 to 0.0106. Fig. 10(b) shows the numerical result with the linear fitting: $\log(L^*) = 0.3506\log(\varepsilon) - 1.2793$. Here, we have a good agreement with the theoretical scaling factor, 1/3.

4.12. Two-dimensional experiment

To validate the proposed formula $h = L^*/m$, we perform the simulation of phase separation on the two-dimensional domain $\Omega = (0,L)^2$. Fig. 11(a)–(c) show the lamellar pattern with different spatial step sizes $h = 0.375/10$, $0.375/20$, and $0.375/40$, respectively. For this numerical test, we use $\Delta t = 0.1$, $\alpha = 100$, $\varepsilon = 1/(20\sqrt{2})$,

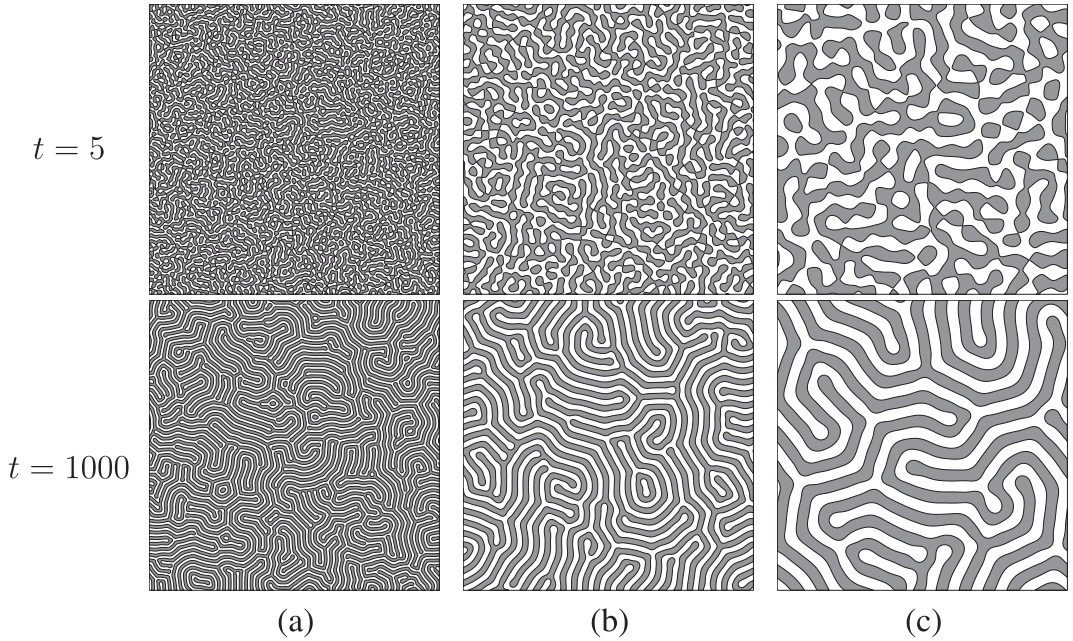

Fig. 11. Lamellar pattern with (a) $h = 0.375/10$, (b) $h = 0.375/20$, and (c) $h = 0.375/40$. $\Delta t = 0.1$, $\alpha = 100$, $\varepsilon = 1/(20\sqrt{2})$, 512×512 mesh grid, $L = 512$ h, and $\overline{\phi} = 0$ are used. First and second rows represent the numerical results at $t = 5$ and $t = 1000$, respectively.

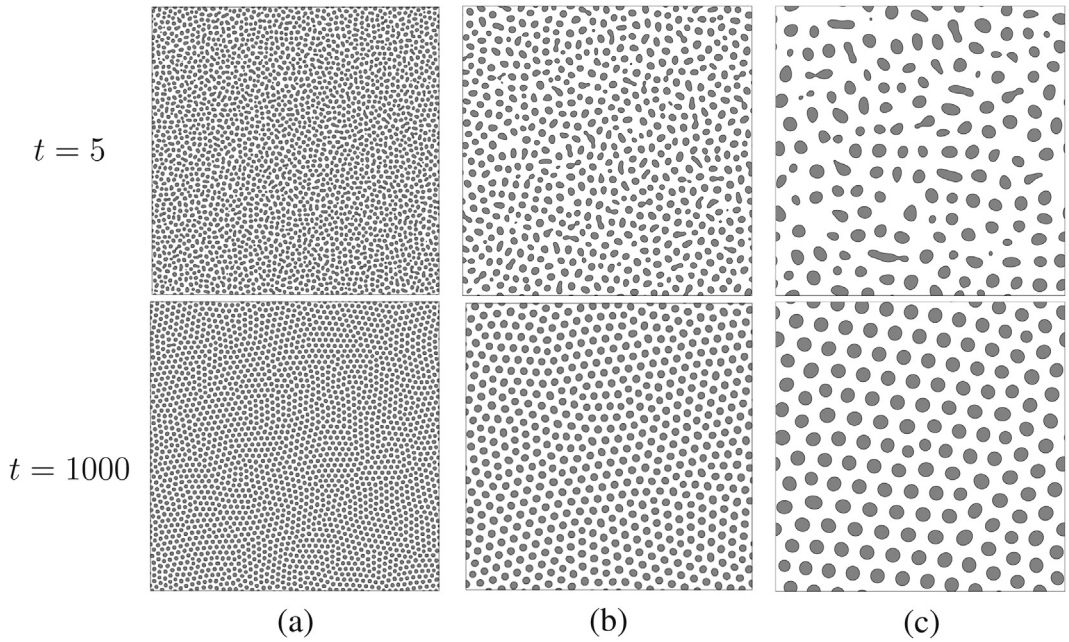

Fig. 12. Hexagonal pattern with (a) $h = 0.31/10$, (b) $h = 0.31/20$, and (c) $h = 0.31/40$. Parameters are used as $\Delta t = 0.1$, $\alpha = 100$, $\varepsilon = 1/(30\sqrt{2})$, 512×512 mesh grid, $L = 512$ h, and $\overline{\phi} = -0.3$. First and second rows represent the numerical results at $t = 5$ and $t = 1000$, respectively.

512×512 mesh grid, and $L = 512$ h with an initial condition $\phi(x,y,0) = 0.15$ rand(x,y). In Fig. 11, first and second rows represent the numerical results at $t = 5$ and $t = 1000$, respectively. By the proposed formula $h = L^*/m$, we can expect approximately $512/m$ waves along the one-axis. As can be seen in the second row of Fig. 11(a)–(c), have approximately 50, 25, 12 periodic waves along the one-axis, respectively.

Now, we consider the hexagonal pattern with different spatial step sizes. For the numerical test, we use $\varepsilon = 1/(30\sqrt{2})$, $\alpha = 100$, 512×512 mesh grid, and $L = 512$ h. The initial condition is set as $\phi(x,y,0) = -0.3+0.15$ rand (x,y). Fig. 12(a)–(c) represent the temporal evolution with $h = 0.31/10$, $0.31/20$, and $0.31/40$, respectively. In Fig. 12(a)–(c), results at $t = 1000$ have approximately 50, 25, 12 periodic waves along the one-axis, respectively.

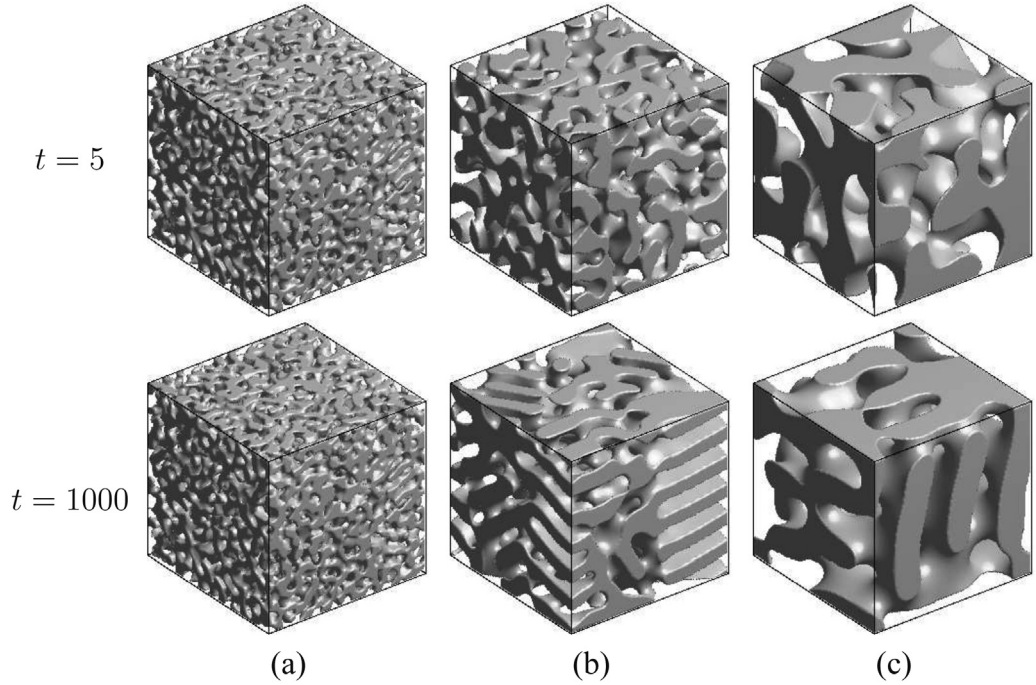

Fig. 13. Lamellar pattern with (a) $h = 0.375/10$, (b) $h = 0.375/20$, and (c) $h = 0.375/40$. Parameters are $\Delta t = 0.1$, $\alpha = 100$, $\varepsilon = 1/(20\sqrt{2})$, $128 \times 128 \times 128$ mesh grid, $L = 128$ h, and $\overline{\phi} = 0$. First and second rows represent the numerical results at $t = 5$ and $t = 1000$, respectively.

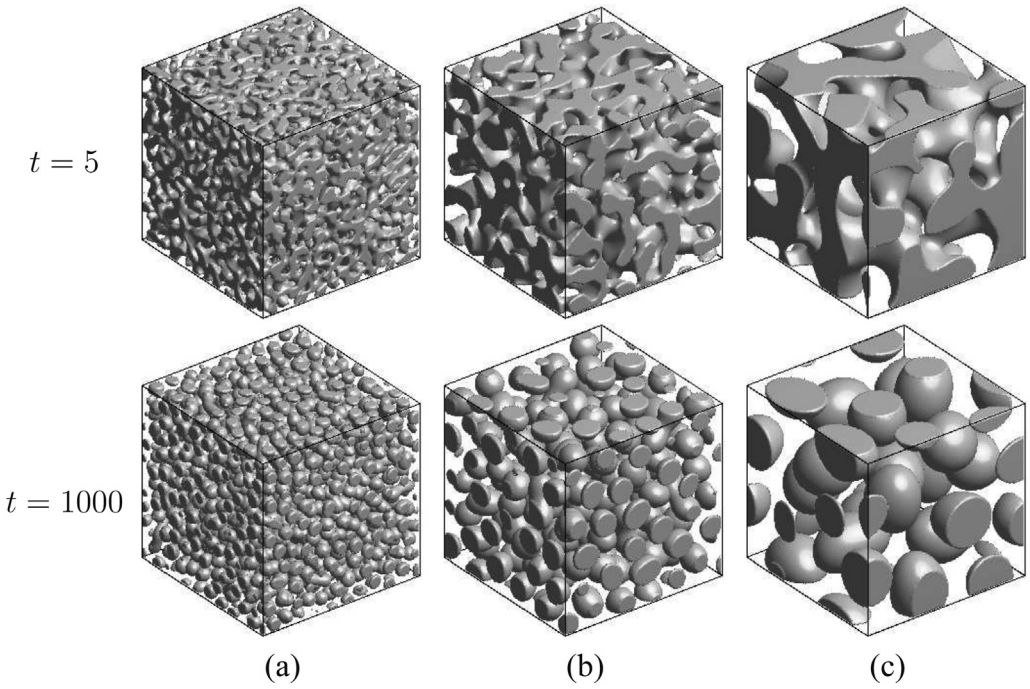

Fig. 14. Spherical pattern with (a) $h = 0.258/10$, (b) $h = 0.258/20$, and (c) $h = 0.258/40$. Parameters are $\Delta t = 0.1$, $\alpha = 200$, $\varepsilon = 1/(30\sqrt{2})$, $128 \times 128 \times 128$ mesh grid, and $\overline{\phi} = -0.3$. First and second rows represent the numerical results at $t = 5$ and $t = 1000$, respectively.

4.13. Three-dimensional experiment

In this section, we perform the simulation of phase separation on the three-dimensional domain $\Omega = (0,L)^3$. We simulate lamellar pattern with different spatial step sizes $h = 0.375/m$, where $m = 10,20$, and 40. Parameters are $\Delta t = 0.1$, $\alpha = 100$, $\varepsilon = 1/(20\sqrt{2})$, and $L = 128$ h. And the initial condition is $\phi(x,y,z,0) = 0.15$ rand(-x,y,z) on $128 \times 128 \times 128$ mesh grid. We observe that (a), (b), and (c) in the second row of Fig. 13 have approximately 12, 6, and 3 periodic waves along the one-axis, respectively.

Fig. 14(a)–(c) show the spherical patterns with $h = 0.258/m$, $m = 10$, 20, and 40, respectively. Here, we use $\alpha = 200$, $\varepsilon = 1/(30\sqrt{2})$, and $\overline{\phi} = -0.3$. In the second row of Fig. 14, we see that (a), (b), and (c) have approximately 12, 6, and 3 periodic waves along the one-axis, respectively.

5. Conclusions

We proposed a robust and accurate numerical algorithm for calculating the energy-minimizing wavelengths of equilibrium states in diblock copolymers. The mathematical model for diblock copolymers is the nonlocal Cahn–Hilliard equation, which consists of local and nonlocal terms associated with short- and long-range interactions, respectively. We used the linearly stabilized splitting-type scheme with a semi-implicit Fourier spectral method to solve the governing equation. To find energy-minimizing wavelengths of the equilibrium states, we considered both PDE and ODE approaches. The results from these methods were identical, which confirms the accuracy of the proposed algorithm. The numerical results indicate that (1) the wavelength becomes shorter as the value of the long-range interaction parameter increases; (2) the wavelength increases with the interfacial energy coefficient value; (3) the most unstable wavelength given by the linear stability analysis is different from the energy-minimizing wavelength as shown in Fig. 6(c); (4) numerical equilibrium states can have non-energy minimizing wavelengths (Fig. 6(d)). We also proposed a simple and powerful formula: $h = L^*/m$, which is very useful in the computational simulations for the physical experiments. For example, it could be used in setting an initial domain size for the algorithm of simulated annealing in order to escape from certain metastable states [45]. Two- and three-dimensional numerical results were presented validating the usefulness of the formula without trial and error or ad hoc processes.

Acknowledgments

The first author (D. Jeong) was supported by a Korea University Grant. The corresponding author (J.S. Kim) acknowledges the support of the MSIP (Ministry of Science, Ict & future Planning).

References

[1] C. Singh, M. Goulian, A.J. Liu, G.H. Fredrickson, Phase behavior of semiflexible diblock copolymers, Macromol 27 (1994) 2974–2986.
[2] F. Liu, N. Goldenfeld, Dynamics of phase separation in block copolymer melts, Phys. Rev. A 39 (1989) 4805–4810.
[3] R. Choksi, M.A. Peletier, J.F. Williams, On the phase diagram for microphase separation of diblock copolymers: an approach via a nonlocal Cahn–Hilliard functional, SIAM J. Appl. Math. 69 (2009) 1712–1738.
[4] F.S. Bates, G.H. Fredrickson, Block copolymers-designer soft materials, Phys. Today 52 (1999) 32–38.
[5] I.W. Hamley, The Physics of Block Copolymers, Oxford University Press, New York, 1998, p. 24.
[6] M. Imai, K. Sakai, M. Kikuchi, K. Nakaya, A. Saeki, T. Teramoto, Kinetic pathway to double-gyroid structure, J. Chem. Phys. 122 (2005) 214906.
[7] M. Seul, D. Andelman, Domain shapes and patterns: the phenomenology of modulated phases, Science 267 (1995) 476–483.
[8] Y.S. Joseph, S. Kim, Q. Zhang, R. Hoogenboom, J.D. Hong, Multilayer films composed of a thermoresponsive cationic diblock copolymer and a photo-responsive dye, Polymer 54 (2013) 4894–4901.
[9] A.T. Lorenzo, M.L. Arnal, A.J. Müller, A. Boschetti de Fierro, V. Abetz, Confinement effects on the crystallization and SSA thermal fractionation of the PE block within PE-*b*-PS diblock copolymers, Eur. Polym. J. 42 (2006) 516–533.
[10] P.A. George, J.J. Cooper-White, Kinetically constrained block copolymer self-assembly a simple method to control domain size, Eur. Polym. J. 45 (2009) 1065–1071.

[11] S. Akasaka, T. Okamoto, T. Osaka, T. Matsushita, H. Hasegawa, 3D analysis of the lattice defects in the gyroid network structure of a block copolymer/homopolymer blend – the line-like defects in the gyroid network structure, Eur. Polym. J. 479 (2011) 651–661.
[12] B. Nandan, B.K. Kuila, M. Stamm, Supramolecular assemblies of block copolymers as templates for fabrication of nanomaterials, Eur. Polym. J. 47 (2011) 584–599.
[13] D. Borah, C.D. Simao, R. Senthamaraikannan, S. Rasappa, A. Francone, O. Lorret, M. Salaun, B. Kosmala, N. Kehagias, M. Zelsmann, C.M. Sotomayor-Torres, M.A. Morris, Soft-graphoepitaxy using nanoimprinted polyhedral oligomeric silsesquioxane substrates for the directed self-assembly of PS-*b*-PDMS, Eur. Polym. J. 49 (2013) 3512–3521.
[14] B.M.D. O'Driscoll, R.A. Kelly, M. Shaw, P. Mokarian-Tabari, G. Liontos, K. Ntetsikas, A. Avgeropoulos, N. Petkov, M.A. Morris, Achieving structural control with thin polystyrene-b-polydimethylsiloxane block copolymer films: the complex relationship of interface chemistry, annealing methodology and process conditions, Eur. Polym. J. 49 (2013) 3445–3454.
[15] O. Karagollu, M. Gorur, A. Turkan, B. Sengez, F. Gode, F. Yilmaz, A novel amperometric glucose biosensor based on poly(glycidylmethacrylate-co-(3-thienylmethylmethacrylate)), Curr. Appl. Phys. 13 (2013) 725–730.
[16] M.-S. Jeong, J.H. Kim, J.-H. Ko, Y.H. Ko, K.J. Kim, Pressure dependence of acoustic behaviors and refractive index of amorphous Kel F-800 copolymer studied by Brillouin spectroscopy, Curr. Appl. Phys. 13 (2013) 1774–1777.
[17] A. Aksimentiev, M. Fialkowski, R. Holyst, Ultrafast dynamics and spectroscopy of bacterial photosynthetic reaction centers, Adv. Chem. Phys. 121 (2002) 1–88.
[18] M. Bahiana, Y. Oono, Cell dynamical system approach to block copolymers, Phys. Rev. A 41 (1990) 6763–6771.
[19] J.W. Cahn, J.E. Hilliard, Free energy of a nonuniform system. I. Interfacial free energy, J. Chem. Phys. 28 (1958) 258.
[20] P.C. Fife, Models for phase separation and their mathematics, Electron. J. Diff. Equ. 48 (2000) 1–26.
[21] M.E. Gurtin, On a theory of phase transitions with interfacial energy, Arch. Ration. Mech. Anal. 87 (1985) 187–212.
[22] O.V. Borisov, E.B. Zhulina, Theory of self-assembly of triblock ter-polymers in selective solvent towards corona-compartmentalized (Janus) micelles, Polymer 54 (2013) 2043–2048.
[23] L. Leibler, Theory of microphase separation in block copolymers, Macromol 13 (1980) 1602–1617.
[24] T. Ohta, K. Kawasaki, Equilibrium morphology of block copolymer melts, Macromol 19 (1986) 2621–2632.
[25] L. Modica, The gradient theory of phase transitions and the minimal interface criterion, Arch. Ration. Mech. Anal. 98 (1987) 123–142.
[26] T. Teramoto, Y. Nishiura, Morphological characterization of the diblock copolymer problem with topological computation, Jpn. J. Ind. Appl. Math. 27 (2010) 175–190.
[27] F.A. Detcheverry, D.Q. Pike, U. Nagpal, P.F. Nealey, J.J. de Pablo, Theoretically informed coarse grain simulations of block copolymer melts: method and applications, Soft Matter 5 (2009) 4858–4865.
[28] T.B. Martin, A. Seifpour, A. Jayaraman, Assembly of copolymer functionalized nanoparticles: a Monte Carlo simulation study, Soft Matter 7 (2011) 5952–5964.
[29] C.A. Mujica-Martinez, J.C. Arce, Mini-bandstructure tailoring in pi-conjugated periodic block copolymers using the envelope crystalline-orbital method, Int. J. Quantum Chem. 110 (2010) 2532–2540.
[30] K.Ø. Rasmussen, G. Kalosakas, Improved numerical algorithm for exploring block copolymer mesophases, J. Polym. Sci. Part B Polym. Phys. 40 (2002) 1777–1783.
[31] L.T. Yan, E. Maresov, G.A. Buxton, A.C. Balazs, Self-assembly of mixtures of nanorods in binary, phase-separating blends, Soft Matter 7 (2011) 595–607.
[32] M. Pinna, A.V. Zvelindovsky, Large scale simulation of block copolymers with cell dynamics, Eur. Phys. J. B 85 (2012) 1–18.
[33] A.W. Bosse, Phase-field simulation of long-wavelength line edge roughness in diblock copolymer resists, Macromol. Theory Simul. 19 (2010) 399–406.
[34] J.G.E.M. Fraaije, S.K. Nath, K. Remerie, J. Groenewold, Phase evolution theory for polymer blends with extreme chemical dispersity: parameterization of DDFT simulations and application to poly (propylene) impact copolymers, Macromol. Theory Simul. 20 (2011) 133–145.
[35] M. Pinna, I. Pagonabarraga, A.V. Zvelindovsky, Modeling of block copolymer/colloid hybrid composite materials, Macromol. Theory Simul. 20 (2011) 769–779.
[36] J.S. Meena, P.P. Thankachan, Theoretical studies of the ring opening metathesis reaction of 3,3-dimethyl cyclopropene with molybdenum catalyst, Comp. Theor. Chem. 1024 (2013) 1–8.
[37] E. Yildirim, M. Yurtsever, The role of diisocyanate and soft segment on the intersegmental interactions in urethane and urea based segmented copolymers: a DFT study, Comp. Ther. Chem. 1035 (2014) 28–38.
[38] D. Wang, X. Zhang, W. Ding, X. Zhao, Z. Geng, Density functional theory design and characterization of D-A-A type electron donors with narrow band gap for small-molecule organic solar cells, Comp. Theor. Chem. 1029 (2014) 68–78.
[39] J. Qin, G.S. Khaira, Y. Su, G.P. Garner, M. Miskin, H.M. Jaeger, J.J. de Pablo, Evolutionary pattern design for copolymer directed self-assembly, Soft Matter 9 (2013) 11467–11472.
[40] F. Drolet, G.H. Fredrickson, Combinatorial screening of complex block copolymer assembly with self-consistent field theory, Phys. Rev. Lett. 83 (1999) 4317.
[41] J.A. Pople, D.L. Beveridge, N.S. Ostlund, Recent progress in approximate self-consistent-field theory, Int. J. Quantum Chem. 1 (1967) 293–305.
[42] R. Choksi, X. Ren, On the derivation of a density functional theory for microphase separation of diblock copolymers, J. Stat. Phys. 113 (2003) 151–176.
[43] A. Segatti, On the hyperbolic relaxation of the Cahn–Hilliard equation in 3D: approximation and long time behaviour, Math. Mod. Meth. Appl. Sci. 17 (2007) 411–437.
[44] I. Ohnishi, Y. Nishiura, M. Imai, Y. Matsushita, Analytical solutions describing the phase separation driven by a free energy functional containing a long-range interaction term, Chaos 9 (1999) 329–341.
[45] R. Choksi, M. Maras, J.F. Williams, 2D phase diagram for minimizers of a Cahn–Hilliard functional with long-range interactions, SIAM J. Appl. Dyn. Syst. 10 (2011) 1344–1362.
[46] Y. Nishiura, I. Ohnishi, Some mathematical aspects of the micro-phase separation in diblock copolymers, Phys. D. 84 (1995) 31–39.
[47] D.J. Eyre, An Unconditionally Stable One-step Scheme for Gradient Systems, 1998. Unpublished article, www.math.utah.edu/~eyre/research/methods/stable.ps.
[48] L.Q. Chen, J. Shen, Applications of semi-implicit Fourier-spectral method to phase field equations, Comput. Phys. Commun. 108 (1998) 147–158.
[49] J. Zhu, L.Q. Chen, J. Shen, V. Tikare, Coarsening kinetics from a variable-mobility Cahn–Hilliard equation: application of a semi-implicit Fourier spectral method, Phys. Rev. E 60 (1999) 3564.
[50] X.F. Wu, Y.A. Dzenis, Guided self-assembly of diblock copolymer thin films on chemically patterned substrates, J. Chem. Phys. 125 (2006) 174707.
[51] B. Benešová, C. Melcher, E. Süli, An implicit midpoint spectral approximation of nonlocal Cahn–Hilliard equations, SIAM J. Numer. Anal. 52 (2014) 1466–1496.
[52] J. Kim, A numerical method for the Cahn–Hilliard equation with a variable mobility, Commun. Nonlinear Sci. Numer. Simul. 12 (2007) 1560–1571.
[53] D. Lee, J. Huh, D. Jeong, J. Shin, A. Yun, J. Kim, Physical, mathematical, and numerical derivations of the Cahn–Hilliard equation, Comput. Mater. Sci. 18 (2014) 216–225.
[54] J.F. Blowey, M.I.M. Copetti, C.M. Elliott, Numerical analysis of a model for phase separation of a multicomponent alloy, IMA J. Numer. Anal. 16 (1996) 111–139.
[55] J.D. Evans, V.A. Galaktionov, J.R. King, Unstable sixth-order thin film equation: II. Global similarity patterns, Nonlinear 20 (2007) 1843.
[56] J. Kierzenka, J.F. Shampine, A BVP solver based on residual control and the Maltab PSE, ACM Trans. Math. Softw. 27 (2001) 299–316.
[57] J. Kierzenka, L.F. Shampine, A BVP solver that controls residual and error, JNAIAM J. Numer. Anal. Ind. Appl. Math. 3 (2008) 27–41.
[58] J. Kim, Phase-field models for multi-component fluid flows, Commun. Comput. Phys. 12 (2012) 613–661.